Chapter 4

Deformation behaviors in metals and alloys

4.1 Introduction

Deformation in solids is often described as elastic, which is reversible, or plastic, which is non-reversible. In a crystalline solid, the major plastic deformation mechanism is the dislocation movements. However, in a nano-scale single crystal, where dislocations cannot be sustained, the plastic deformation occurs through coherent shearing events, such as slip and twinning. Twinning, in which blocks of a crystal are sheared to alter its orientation, is favored over slip as the temperature of deformation is decreased or the rate of deformation is increased. Under high-strain rate or shock-loading/impact conditions, deformation twinning is observed to be promoted even in high stacking fault energy face centered cubic (FCC) metals and alloys which normally do not readily deform via twinning (Honeycombe, 1984).

The deformation mechanism of metallic glasses is known to be more complicated than the crystalline counterpart. Depending on the temperature and stress conditions, metallic glasses show elastic, viscoelastic, inhomogeneous plastic, or homogeneous plastic deformation behavior (Spaepen, 1977). Especially, metallic glasses show a unique coherent shearing behavior upon yielding, which are localized shear bands. There have been many attempts to explain the shear localization behavior in metallic glasses using descriptions such as compositional disorder (Polk and Turnbull, 1972), shear induced free volume (Spaepen and Turnbull, 1974), or adiabatic heating (Leamy *et al.*, 1972), but is has not yet been completely understood.

In this chapter, we employ MD simulations to investigate the deformation mechanism of metallic glasses and compare it to the deformation mechanism of the crystalline materials. In crystalline materials, it is relatively simple to identify the plastic deformation mechanism. For example, coherent shearing events in crystalline materials, such as twins or slips, alter the crystallographic orientation after yielding. Thus, twins or slips can be easily identified by analyzing the crystallographic structure of the material. However, this simple structural analysis does not work for glasses because there is no well-defined long-range structural order in glasses. Therefore, we introduce a generic method to identify plastic deformation, which is applicable to crystalline and glass materials.

This chapter is organized as follows. First, the deformation experiments on nano-wires will be described and summarized in both crystalline and amorphous cases. Nano-wires are deformed under the constant temperature condition to observe the deformation behavior without adiabatic heating. Next, deformation experiments on notched slabs will be presented and the failure mechanism and the adiabatic heating effect will be discussed.

4.2 Deformation of metallic nano-wires

4.2.1 Simulation methods

A crystalline nano-wire was prepared using a stress-free Cu FCC single crystal at T=300K. A cylindrical geometry was chosen to minimize defect initiation and surface diffusion at a high surface curvature region. To generate a cylindrical geometry, we used a cutoff radius in the x-y plane, while the z-direction is subject to periodic boundary conditions. This leads to a cylindrical nano-wire with a relatively smooth but faceted

surface in the x-y plane and an infinite length in the z-direction (1370 atoms in a unit cell, Fig. 4-1(a)).

After the Cu FCC single crystalline nano-wire is prepared, the wire was equilibrated for 10ps (10,000 MD steps) at T=300K using constant temperature, constant shape (*ThN*) dynamics (Ray and Rahman, 1984, 1985). Then, the uniform tensile strain was applied by straining the sample in the z-direction (Fig. 4-2(a)). The strain is increased in a step-wise pattern at constant temperature T=300K using *ThN* dynamics. At each step, the sample is strained by 0.5% uniformly then allowed to relax over 10ps periods reaching thermodynamic equilibrium. During this period, the stress components s_{ij} were averaged, where $i=x, y,$ and z. The final configuration was used as an input for the next initial configuration and the process is repeated. In this manner, a strain rate of 0.05%/ps is achieved.

Simulations were also performed on a metallic glass nano-wire. To obtain a stable metallic glass model system, we chose a generalized binary alloy system with sufficient atomic size mismatch. By simply varying the atomic size mismatch, one can obtain a relatively stable glass system compared to a mono-atomic system (Egami and Waseda, 1984; Lee, 2003). For this purpose, we chose Cu as the base material. As the second component, we introduced an artificial Cu-like atom, Cu^*, which has the same force-field parameters except for its size parameter, in other words, its atomic radius. The atomic size ratio of Cu^* to Cu was set at 1.13 (Lee, 2000), corresponding to the Ag-Cu alloy system, which is known to be a good glass former. The Q-SC force field parameters used in this study are shown in Table 4-1.

By substituting Cu atoms with Cu^* in the single Cu crystalline nano-wire, we obtained the $Cu^*_{50}Cu_{50}$ random FCC crystalline nano-wire. To relieve the local atomic stress induced by the larger atom Cu^*, we uniformly increased the cell size in the x, y and z directions and found a stress free cell size ($L_{x,y,z}$=3.9 nm) at T=300K. After the stress free $Cu^*_{50}Cu_{50}$ random FCC nano-wire is prepared, we performed heating and cooling simulations to obtain a realistic glass structure. First, we heat the $Cu^*_{50}Cu_{50}$ random FCC nano-wire from 300K to 1600K using a 4×10^{12} K/s heating rate. At T=1600K, the sample is completely molten and in the equilibrium liquid state. Then, we cool the sample down to 300K using the same cooling rate (4×10^{12} K/s). The sample freezes into a glass at or above T=500K. The prepared $Cu^*_{50}Cu_{50}$ glass nano-wire is shown in Fig. 4-1(b). It has a cylindrical geometry, which minimizes the surface energy and shows no long range order (Fig. 4-7(b)). After equilibrating the $Cu^*_{50}Cu_{50}$ glass nano-wire for 10ps at T=300K, we applied a strain rate of 0.05%/ps using the same method as was used for the crystalline system. The snapshots of the $Cu^*_{50}Cu_{50}$ glass nano-wire during the deformation process are shown in Fig. 4-2(b).

4.2.2 Crystalline nano-wire deformation

Fig. 4-3 shows a stress-strain curve for the Cu crystalline nano-wire of strain rate 0.05%/ps at T=300K. When the strain is small, the deformation leads to a linear increase in stress (elastic deformation). The crystalline wire shows an elastic response up to 8% strain (the yield point) and then plastically deforms, accompanying a sudden decrease in stress by releasing the stored elastic energy (e.g., strain 8% to 10%). In general, the plastic deformation in crystalline materials occurs through a dislocation movement or a

generation of local defects, such as twin or slip (Honeycombe, 1984). However, a dislocation cannot be sustained in a nano-sized single crystal. Therefore, the possible plastic deformation mechanism is twin and slip.

To better understand the deformation mechanism between 8% to 10% strain, we examined the crystalline structure of the wire during these strain states. Fig. 4-4 shows the (011) crystallographic projection of the Cu single crystalline wire. The structure is color-coded to emphasize the structural change, where a larger sphere indicates a group of neighbor atoms on (111) and ($11\underline{1}$) planes. Up to the yield point, the original crystalline structure is maintained (Fig. 4-4(a) and(b)). After passing the yield point, we observe a slip in the {111} plane, which induces a slight step in the wire surface (Fig 4-4(c)). Immediately after the slip, the twin is formed at the surface step generated by the previous slip process (Fig 4-4(d)). Therefore, we conclude that the sharp drop in the strain-stress curve (strain 8% to 10%) is due to the formation of twin and slip.

After releasing the stored elastic energy by generating local defects (twin and slip), the sample shows elastic behavior (strain 10% to 14.5%) again until it reaches a new yield point. The Young's modulus, which is the slope of the stress-strain curve in the elastic region, is approximately constant in all elastic loading regions. The plastic deformation proceeds with the successive slip in the twin and twin boundaries and leads to the failure of the material at strain 91.0%.

4.2.3 Amorphous nano-wire deformation

The stress-strain curve of a $Cu^{*}_{50}Cu_{50}$ amorphous nano-wire is shown in Fig. 4-5. Compared to its crystalline counterpart, the amorphous nano-wire shows a more

complicated stress-strain response. The elastic deformation and plastic deformation are not well defined and the stress-strain curve shows more frequent stress changes due to the intrinsic structural randomness. After increasing in a linear fashion up to strain 3.5% (yield point), the stress drops and then increases successively. This successive elastic and plastic response in the stress-strain curve, gets more pronounced in the later stage of deformation (strain>50.0%) which is mainly due to flow localization mechanisms, such as necking.

To visualize the structural change in the amorphous nano-wire, atoms are color-coded according to their initial position (strain=0 state) in the z-direction (Fig. 4-6). Thus, the change of the width in the z-direction of the each color-coded block compared to its original width is proportional to the strain. This enables the convenient observation of the inhomogeneity in the strain field. As shown in Fig. 4-6(d), the strain is localized in a relatively narrow region (about 2 out of 10 blocks) and this agrees with the shear localization behavior in metallic glasses.

4.2.4 Inter-atomic distance change (D_{ij}) analysis

This simple visualization technique cannot provide detailed information about the atomistic deformation processes of the amorphous system because there is no well-defined long-range structural order in glasses, unlike the crystalline counterpart. To overcome this limitation, we introduce an improved generic method to capture the local defects and the atomistic deformation processes by identifying the elastically deformed region and the plastically deformed region, which can be used for both glass and crystalline materials.

To separate elastic deformation and plastic deformation events, we take advantage of the fact that the inter-atomic distances change very little during the elastic deformation. To track the change in inter-atomic distance, we introduce a parameter Δ_{ij},

$$\Delta_{ij}(t) = \left| r_{ij}(t) - r_{ij}(0) \right| \tag{4-1}$$

where $r_{ij}(t)$ is the distance between atom i and j at time t. Atomic pair i and j are chosen as every nearest neighbor pair in the system. Two atoms are nearest neighbors if they are within a specified cutoff distance of each other. We employ a cutoff distance as the first minimum in the radial distribution function (RDF). This first nearest neighbor cutoff is held constant as 3.049Å for the Cu crystalline wire (Fig. 4-7(a)) throughout the deformation process and 3.543Å for the $Cu^{*}_{50}Cu_{50}$ amorphous wire (Fig. 4-7(b)).

Fig. 4-8 shows the Δ_{ij} probability distribution function for the Cu single crystalline nano-wire at various strain states. The Δ_{ij} probability distribution function is normalized so that the area under the curve becomes 1.0. In general, the inter-atomic distance in the direction of the tensile loading (z-direction) increases as the strain increases. However, the elongation in the tensile loading direction is accompanied by a contraction in the two perpendicular transverse directions (x and y directions), which results from the Poisson effect at the atomic level; hence, the inter-atomic distance decreases in x and y directions. In addition, thermal vibrations (T=300K) and the existence of a free surface contribute to Δ_{ij}. Therefore, the Δ_{ij} shows a distribution as shown in Fig. 4-8.

The atomic displacement distribution is monotonic if the wire is elastically deformed (Fig. 4-8 at strain 8%). However, as the strain bypasses the elastic limit, the atomic strain distribution deviates from the monotonic distribution and shows additional

peaks in the large atomic strain value regime (Fig. 4-8 at strain 8.5% and above). Intuitively, one can surmise that these additional peaks are due to plastic deformation. To determine the validity of this assumption, we examined the atomic pairs that have large values of Δ_{ij}>0.75Å. This value is chosen as the point that separates the first and second peaks in the distribution function (Fig. 4-8). We chose strain=10% as the test case because we are able to discern the plastically deformed region by comparing the crystallographic orientation obtained previously (Fig. 4-4(f)). The pairs of atoms with Δ_{ij}>0.75Å are shown as small spheres and the rest as large spheres in Fig. 4-9(c). We find that this method successfully separates the plastically deformed region and the elastically deformed region by capturing both slip and twin. Therefore, in the Cu single crystalline wire, the elastically deformed region and the plastically deformed region can be identified using Δ_{ij} and the threshold value is about 0.75Å. One interesting observation is that the threshold value for plastic deformation (0.75Å) is about 25% of the first neighbor distance 3.049Å, which is similar to the Lindemann melting formula. This suggests that the mechanical instability of a crystal and melting are closely related phenomena.

The same procedure was performed on the metallic glass nano-wire. The D_{ij} distribution function is given in Fig. 4-10. Due to its structural randomness, some atomic pairs have higher Δ_{ij} values; thus, there is a long tail in the distribution function. Similar to the result of crystalline case, it shows additional peaks if the system undergoes a plastic deformation. The threshold value for plastic deformation is found to be 1.0Å. Using this criterion, the plastically deformed region and the elastically deformed regions are visualized in Fig. 4-11. Here, the plastically deformed region is shown as small

spheres and the elastically deformed region is shown as large spheres. In the early stage of deformation (Fig. 4-11(a)), the metallic glass wire shows global plastic deformation, which can be compared to mechanical annealing. At intermediate strain (Fig. 4-11(b)), the plastic deformation starts to localize and it appears as a band form approximately 45 degrees to the loading axis (the direction of maximum resolved shear stress). This is a generally observed phenomena in tensile experiments with metallic glasses (Choi-Yim, 1999; Lu, 2002). At high strain (Fig. 4-11(c)), the wire shows necking and the plastic deformation is very localized at the necked area. The necking is more fully developed as the strain increases and leads to the failure of the sample. The neck is usually symmetric in shape, indicating that multiple slips are operative within it due to the geometrical symmetry of the wire. At this stage of the tensile process, the gross plastic deformations are localized to the diffusely necked region.

This method was further generalized for structurally complicated systems (e.g., polycrystalline material or amorphous material) or multi-directional loading conditions by creating an algorithm that automatically partitions the system into clusters of elastically deformed atoms. To implement this idea, we used a simulated annealing method using atomic strain (Δ_{ij}) as a parameter (Newman, 1999). Simulated annealing finds the partition of the system that minimizes the cost function,

$$C = \sum_{k} \sum_{i,\, j \in k} f(\Delta_{ij}). \qquad (4\text{-}2)$$

Here, k is the index for clusters and i, j are the index for atoms. $f(\Delta_{ij})$ is defined to be negative if Δ_{ij} is smaller than the threshold value r_c for the plastic deformation. If Δ_{ij} is bigger than r_c, $f(\Delta_{ij})$ becomes positive. Therefore, to minimize the cost function, the method partitions the system as elastically deformed clusters by excluding the plastically

deformed atomic pairs. The transition between negative to positive values is described smoothly using the Fermi function. $f(\Delta_{ij})$ increases in a linear fashion at large Δ_{ij} to accelerate the partitioning processes by assigning large values to $f(\Delta_{ij})$. The functional forms are

$$f(\Delta_{ij}) = 1 - \frac{2}{\exp(20.0(\Delta_{ij} - r_c)) + 1.0} \qquad \text{if } D_{ij} < 1.2\text{Å} \qquad (4\text{-}3)$$

and

$$f(\Delta_{ij}) = 4(\Delta_{ij} - 1.2) + 1 \qquad \text{if } D_{ij} = 1.2\text{Å}. \qquad (4\text{-}4)$$

r_c is set to 0.75Å for the crystalline nano-wire and 1.00Å for the amorphous nano-wire. Fig. 4-12 shows $f(D_{ij})$ in each case and data obtained using strain=10% case for crystalline nano-wire and strain=32% for amorphous nano-wire are plotted together.

Using this method, the nano-wires were partitioned into elastically deformed clusters. Fig. 4-13 shows the result of this algorithm on the crystalline nano-wire structure at strain=10%, where we previously observed the presence of slip and twin. This method partitioned the sample into 5 clusters. Two major clusters have 757 atoms and 609 atoms (note that the total number of atoms in the system is 1370), presented with red and green colors, respectively. From this, it is clear that the algorithm successfully partitions the system into the elastically deformed clusters by having twin and slip as their boundaries.

The amorphous nano-wire was partitioned using this method, the result of which is shown in Fig. 4-14. We concentrate our analysis on the region of strain from 24.0% to 32.0% because it most closely demonstrates elastic behavior (24.0%-29.0%) and plastic behavior (29.0%-32.0%) in strain-stress curve (Fig. 4-5). We obtain Δ_{ij} by calculating

the first nearest neighbor distance change as compared to the strain 24.0% state. The cluster analysis partitions the wire into 22 clusters. Except for the two major clusters of size 839 atoms and 434 atoms, the others are tens of atoms or smaller. The boundary of the obtained clusters generally coincides with the plastically deformed region in Fig. 4-11(b). Note that there are two major clusters facing each other at 45 degrees, suggesting plastic deformation mostly happens in this 45 degree interfaces between clusters. The advantage of this analysis over simple observation, such as Fig. 4-11, is that this analysis provides more rigorous data in identifying the plastically deformed regions and the elastically deformed regions in a complex system.

4.2.5 Deformation-induced changes in local order

During the deformation process, the global structural properties of both crystal and glass were maintained (Fig. 4-7(a) and (b)). However, to see changes in the local structural properties, we employed the Honeycutt-Andersen (HA) analysis, introduced in Chapter 3. In the crystalline nano-wire, the fraction of the 1421 pairs, which is a characteristic of FCC structure, decreases when plastic deformation occurs, while the 1422 and 2331 pair fractions increase, which is a characteristic of HCP structure. Therefore, the plastic deformation of a FCC crystalline wire generates a HCP structure by forming twins and slips. On the contrary, the amorphous nano-wire does not show any dramatic change in the HA pair fraction. The 1551 and 2331 pairs decrease at strain below 10%, but recover by strain 20% and remain almost constant during the deformation.

4.2.6 Effects of strain rate and temperature

The stress-strain curves of the amorphous nano-wire at different temperatures and different strain rates are shown in Fig. 4-16 and Fig. 4-17, respectively. In general, amorphous metals deform homogeneously at high temperature and low stress conditions. However, they deform inhomogeneously at low temperature and high stress conditions (Spaepen and Turnbull, 1984). We find that the stress becomes higher as the temperature decreases or the strain rate increases. In particular, the rise and fall in the stress-strain curves become more distinctive as the temperature decreases, indicating the potential of more confined plastic deformation, *i.e.*, inhomogeneous flow. Finally, the stress overshoots and the steady state stress increases as the applied strain rate increases, which agrees with experiments (Lu, 2002).

4.2.7 Conclusions

Using the Q-SC many-body force-field, we use molecular dynamics simulations to study the deformation of metallic nano-wires. The plastic deformation of Cu single crystalline nano-wire at 300K proceeds first by slip and twinning in (111) plane and then only by the slip in the twin boundary, which leads failure of the material. The glass nano-wire shows the plastic deformation, which localizes in 45 degree with respect to the loading axis as the strain increases. As the strain increases more, this localized plastic deformation appears as necking in this experiment due to the symmetry of the cylindrical wire. The necking is more fully developed with the increase of the strain and leads the failure of the material.

4.3 Deformation of metallic nano-slabs

4.3.1 Simulation methods

The computer model of a FCC Cu crystalline nano-slab consists of 61,432 atoms in three dimensions interacting via the Q-SC many-body potential. The configuration of a notched slab is shown in Fig. 4-18(a) and (b). The cell size was determined to satisfy a zero stress condition at T=300K. This leads to a cell with dimensions $288.6 \times 71.4 \times 37.7 \text{Å}^3$ at 300K. The FCC crystal is oriented in such a way that the crack plane is on (010) and the crack front is along the [101] direction. Therefore, the {111} slip planes are 35.2644 degrees with respect to the x-axis.

The computer model of a $Cu^*_{50}Cu_{50}$ metallic glass nano-slab consists of 63,000 atoms in three dimensions (Fig. 4-18(c) and (d)). To obtain a realistic amorphous model specimen, melting and quenching simulations were performed under constant temperature, constant stress (*TtN*) conditions (Ray and Rahman, 1985). This leads to a cell with dimensions $311.9 \times 98.0 \times 39.0 \text{Å}^3$ at T=300K.

The specimen was subject to free boundary conditions in the direction of crack propagation (y direction) and periodic boundary conditions in the x and z directions. The initial configuration for the crack propagation simulation is obtained by thermalizing the notched sample using constant temperature and shape (*ThN*) MD for 5 ps. During thermalization at 300K, the atomic configuration in the bulk is almost frozen, but atoms on the free surface show high mobility. Atoms on the crack surface diffuse to decrease the curvature on the crack site, leading to a lower surface energy (Fig. 4-18 (b) and Fig. 4-18 (d)).

To simulate mode I crack propagation (uni-axial loading), expanding boundary conditions are imposed in the x-direction (Holian and Ravelo, 1995). The cell parameter in the x-direction $L_x(t)$ is increased at every time step such that

$$L_x(t) = L_x(0) + vt = L_x(0) + L_x(0)\dot{e}t, \qquad (4\text{-}5)$$

where $L_x(0)$ is the cell size in x-direction at time t=0, v is the expansion velocity, and $\dot{e}$ is the stain rate. The strain rate used in this study is 0.5%/ps and the cell parameter is increased at every MD step (1 MD step=2fs), which leads to a continuous expansion in the x-direction.

4.3.2 Crystalline nano-slab deformation

The FCC Cu crystalline nano-slab deforms in a ductile fashion and most of the deformation appears to be concentrated around the crack tip and surface. To better understand the microscopic processes during deformation, atoms near the crack tip are shown with different colors, corresponding to their initial x coordinate positions (Fig. 4-19). This shows the rearrangement of atomic structure near the crack tip during deformation. As the strain increases, the crystalline nano-slab shows twins and slips in the (111) planes. The slip initially occurs by the emission of a dislocation from the crack tip and dislocations are successively emitted as the stain increases further.

In order to observe the time evolution of the local quantities such as the local Δ_{ij} and the local temperature, the system is divided with a rectangular grid in the x (36 regions) and y (11 regions) directions. For each region, the averaged local quantities are calculated. Since Δ_{ij} is an inter-atomic quantity, the spatial coordinate is assigned to be the center of mass of atom i and j for the spatial average. Fig. 4-20 shows the contour

map of local Δ_{ij} in the crystalline nano-slab at different strain states. We find that the crystalline nano-slab deforms through the emission of a dislocation and the deformation is localized in the 35.3 degree direction from the crack tip with respect to the loading axis. This agrees with the prediction that plastic deformation occurs on the {111} slip plane system in FCC (Honeycombe, 1984).

The local temperature evolution is also obtained using the same grid dimensions. First, the temperature of each atom is calculated using the atomic velocity. Then, the local temperature was obtained by averaging the atomic temperature over a grid. The local temperature is the highest around the crack tip, where the maximum temperature is T~600K, and correlates with the Δ_{ij} results.

4.3.3 Amorphous nano-slab deformation

The glass nano-slab demonstrates a ductile deformation and the crack becomes blunted as the strain increases. From Fig. 4-22, it can be observed that the most deformation is concentrated around the crack tip. However, it is more difficult to see by eye the well-defined localized deformation of the amorphous nano-slab, as compared to the crystalline case.

Using the local strain map (Fig. 4-23), the localized deformation is captured for the amorphous nano-slab. The deformation is very localized around the crack tip and it grows in a 45º angle from the crack tip with respect to the tensile axis. This localized zone has a thin band type of geometry and the width is about 20-40 Å at strain=20%.

Fig. 4-24 shows the time evolution of the local temperature. From the fact that significant deformation and localization exist even below the glass transition temperature,

the localization of shear is more likely caused by the increase of viscosity (or atomic mobility) associated with increased free volume in the shear bands (strain localized zone), as opposed to adiabatic heating.

4.3.4 Discussion

Inhomogeneous flow in metallic glasses occurs in thin, shear bands, the position of which is determined by the planes of maximum shear stress. Although the plastic strain inside the bands is very large, the overall strain in a tension experiment is small due to the small number of shear bands that form prior to failure.

For small-scale yielding and rapid rates, it is reasonable to use Rice and Levy's model to predict the upper limit of the crack tip temperature increase (Rice, 1969). Rice and Levy's model assumes 100% conversion of the plastic work to local heating and employs the non-hardening plasticity model. In a metallic glass, which shows no work hardening, this assumption is reasonable and the fast strain rate (~10^{15} 1/sec) used in these simulations makes the use of Rice and Levy's model more appropriate. Since the deformation occurs in a ductile fashion and the crack does not show any apparent propagation, the crack is assumed to be stationary. The maximum temperature increase can then be approximated by

$$\Delta T \approx \frac{s_0}{p r C_p}, \tag{4-6}$$

where r is the density, C_p is the specific heat, and s_0 is the tensile yield stress. The measured r is 7142.23 Kg/m^3, C_p is 30 J/mol/K, and s_0 is ~2 GPa for the $Cu^*_{50}Cu_{50}$ metallic glass. This model estimates the maximum temperature increase at the crack tip

to be 189K. Since the simulations were done at T=300K, the crack tip temperature can reach up to 489K, which is agrees with our observation from Fig. 4-24.

4.3.5 Conclusion

Crack propagation in a pre-notched FCC Cu and amorphous nano-slab under uni-axial strain at T=300K is studied using molecular dynamics. The FCC Cu nano-slab deforms by twin formation and dislocation emission from the crack tip and deformation is localized in the (111) plane. In the amorphous nano-slab, deformation is localized in a thin band oriented at a 45º angle with respect to the tensile direction. During the deformation process, local inter-atomic distance change Δ_{ij} and local temperature evolution is directly measured. In particular, the local temperature increment at the crack tip of the amorphous slab shows a good agreement with predictions of the plastic work dissipation as heat. Based on the results that significant deformation and shear localization proceeds below the glass transition temperature, we conclude that the localization of shear in metallic glass is more likely caused by the decrease of viscosity (or the increase of atomic mobility) associated with increased free volume in the shear, rather than adiabatic heating.

References

Choi-Yim, H. (1999). Synthesis and characterization of bulk metallic glass matrix composites, California Institute of Technology.

Egami, T., and Waseda, Y. (1984). Atomic Size Effect on the Formability of Metallic Glasses. J. Non-Cryst. Solids *64*, 113-134.

Holian, B.L., and Ravelo, R. (1995). Fracture Simulations Using Large-Scale Molecular-Dynamics. Physical Review B *51*, 11275-11288.

Honeycombe, R.W.K. (1984). The plastic deformation of metals. Edward Arnold Ltd.

Leamy, H.J., Chen, H.S., and Wang, T.T. (1972). Plastic-Flow and Fracture of Metallic Glass. Metallurgical Transactions *3*, 699.

Lee, H.-J., Cagin, T. C., Johnson, W. L., and Goddard III, W. A. (2003). Criteria for formation of metallic glasses: the role of atomic size ratio. J. Chem. Phys. *in review*.

Lee, H.-J., Qi, Y., Cagin, T. C., Johnson, W. L., and Goddard III, W. A. (2000). Molecular dynamics simulations of supercooled liquid metals and glasses. Mat. Res. Soc. Symp., Boston, *644*, L2.3.1.

Lu, J. (2002). Mechanical behavior of a bulk metallic glass and its composite over a wide range of strain rates and temperatures, California Institute of Technology.

Newman, M.E.J.a.B., G. T. (1999). Monte Carlo Methods in Statistical Physics. Oxford University Press Inc.

Polk, D.E., and Turnbull, D. (1972). Flow of Melt and Glass Forms of Metallic Alloys. Acta Metallurgica *20*, 493-&.

Ray, J.R., and Rahman, A. (1984). Statistical Ensembles and Molecular-Dynamics Studies of Anisotropic Solids. J. Chem. Phys. *80*, 4423-4428.

Ray, J.R., and Rahman, A. (1985). Statistical Ensembles and Molecular-Dynamics Studies of Anisotropic Solids .2. J. Chem. Phys. *82*, 4243-4247.

Rice, J.R.a.L.N. (1969). Local heating by plastic deformation at a crack tip. In: Physics of strengh and plasticity, ed. A. A.S., Cambridge: The M.I.T. Press, 277.

Spaepen, F. (1977). Microscopic Mechanism for Steady-State Inhomogeneous Flow in Metallic Glasses. Acta Metallurgica *25*, 407-415.

Spaepen, F., and Turnbull, D. (1974). Mechanism for Flow and Fracture of Metallic Glasses. Scripta Metallurgica *8*, 563-568.

Spaepen, F., and Turnbull, D. (1984). Metallic Glasses. Annu. Rev. Phys. Chem. *35*, 241-263.

Table 4-1. Force-field parameters for the quantum Sutton-Chen (Q-SC) many-body potential for Cu and Cu*. Note that Cu* has the same force-field parameters except for the lattice constant.

	e(meV)	*c*	*m*	*n*	*a* (A)
Cu	5.7921	84.843	5	10	3.603
Cu*	5.7921	84.843	5	10	4.071

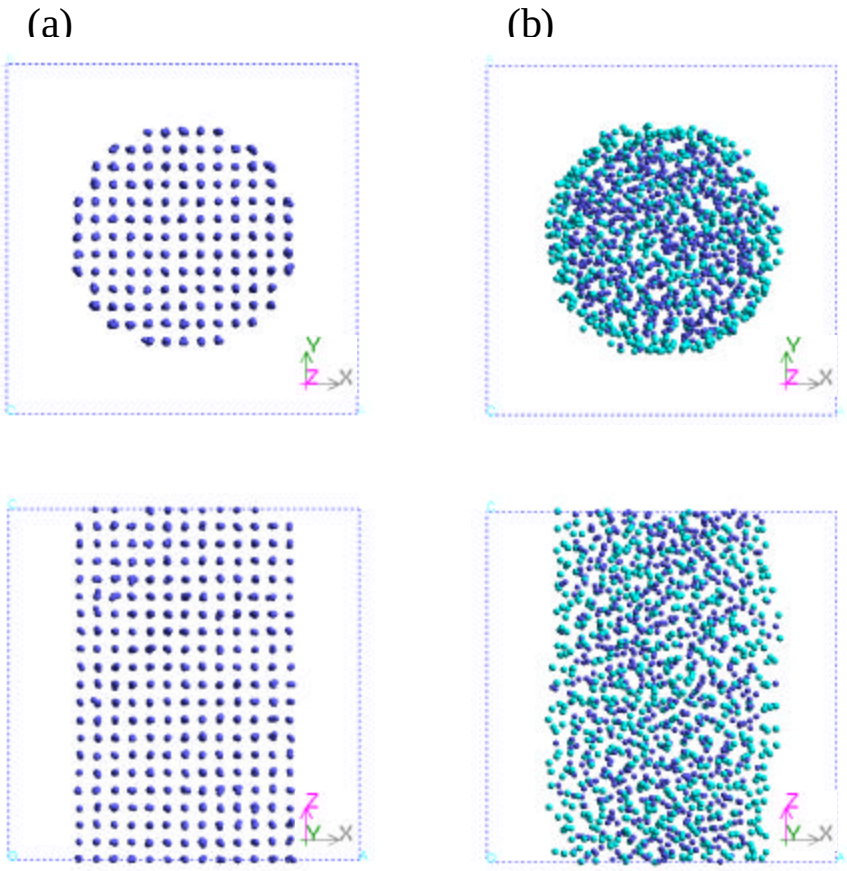

Figure 4-1. The cross section and side view of nano-wires. (a) Cu crystalline wire. The diameter of the crystalline wire is about 2.4nm and the length in the z direction is ~3.6nm. (b) $Cu^{*}_{50}Cu_{50}$ amorphous wire. The diameter of the glass wire is ~2.86nm and the length in z-direction is ~3.9nm.

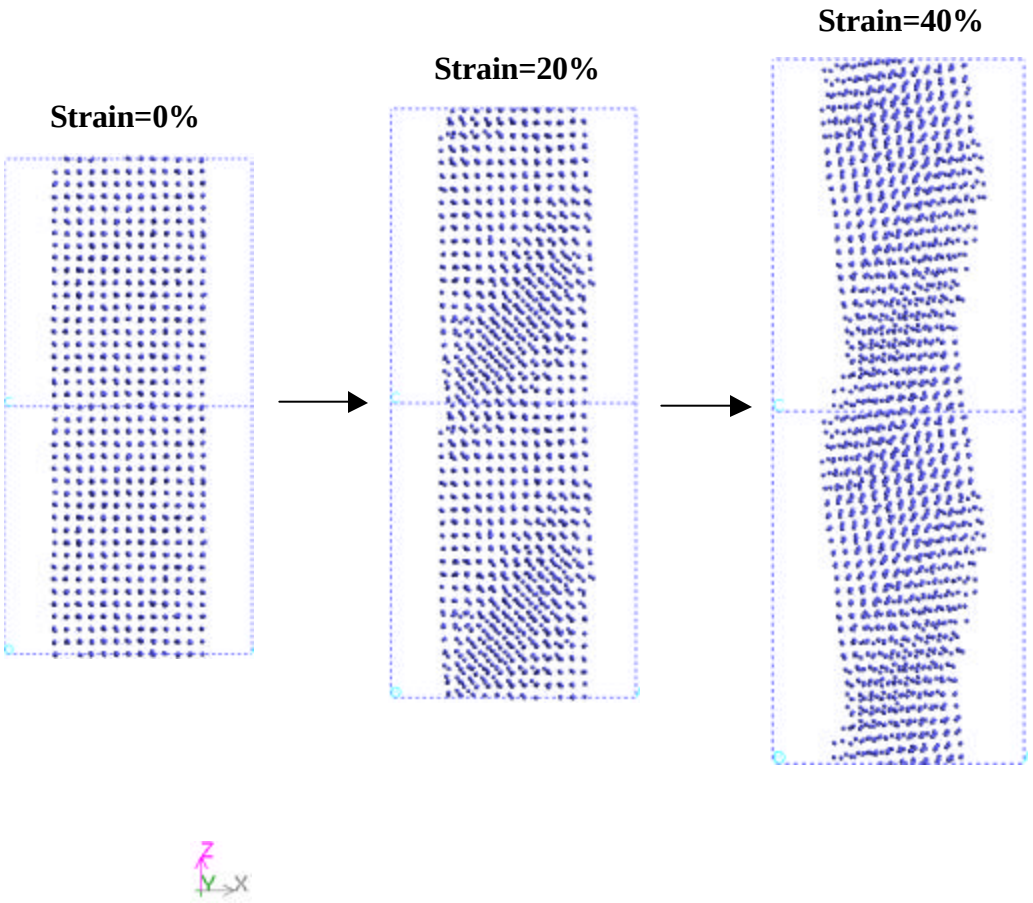

Figure 4-2(a). Snapshots of the Cu crystalline wire at different strain states. The unit cell is duplicated in the z-direction to aid the visualization of the deformation process.

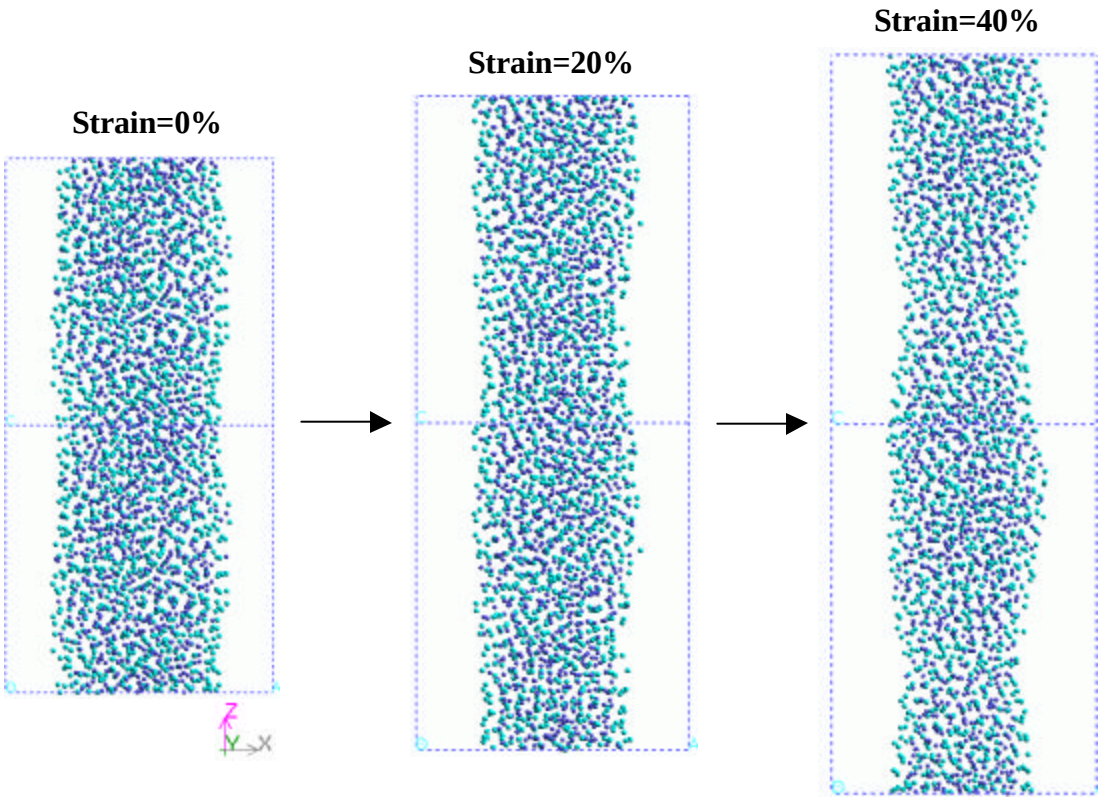

Figure 4-2(b). Snapshots of the $Cu^{*}_{50}Cu_{50}$ amorphous wire at different strain states. The unit cell is duplicated in the z-direction to aid the visualization of the deformation process.

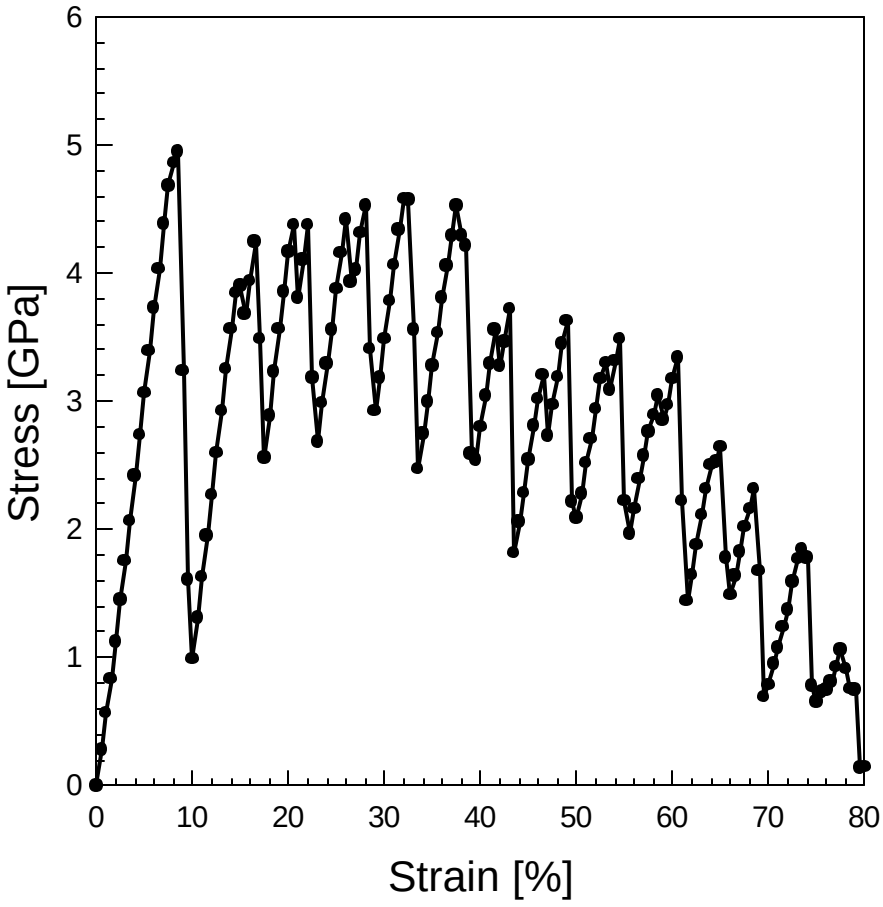

Figure 4-3. The stress-strain curve of the Cu single crystalline nano-wire.

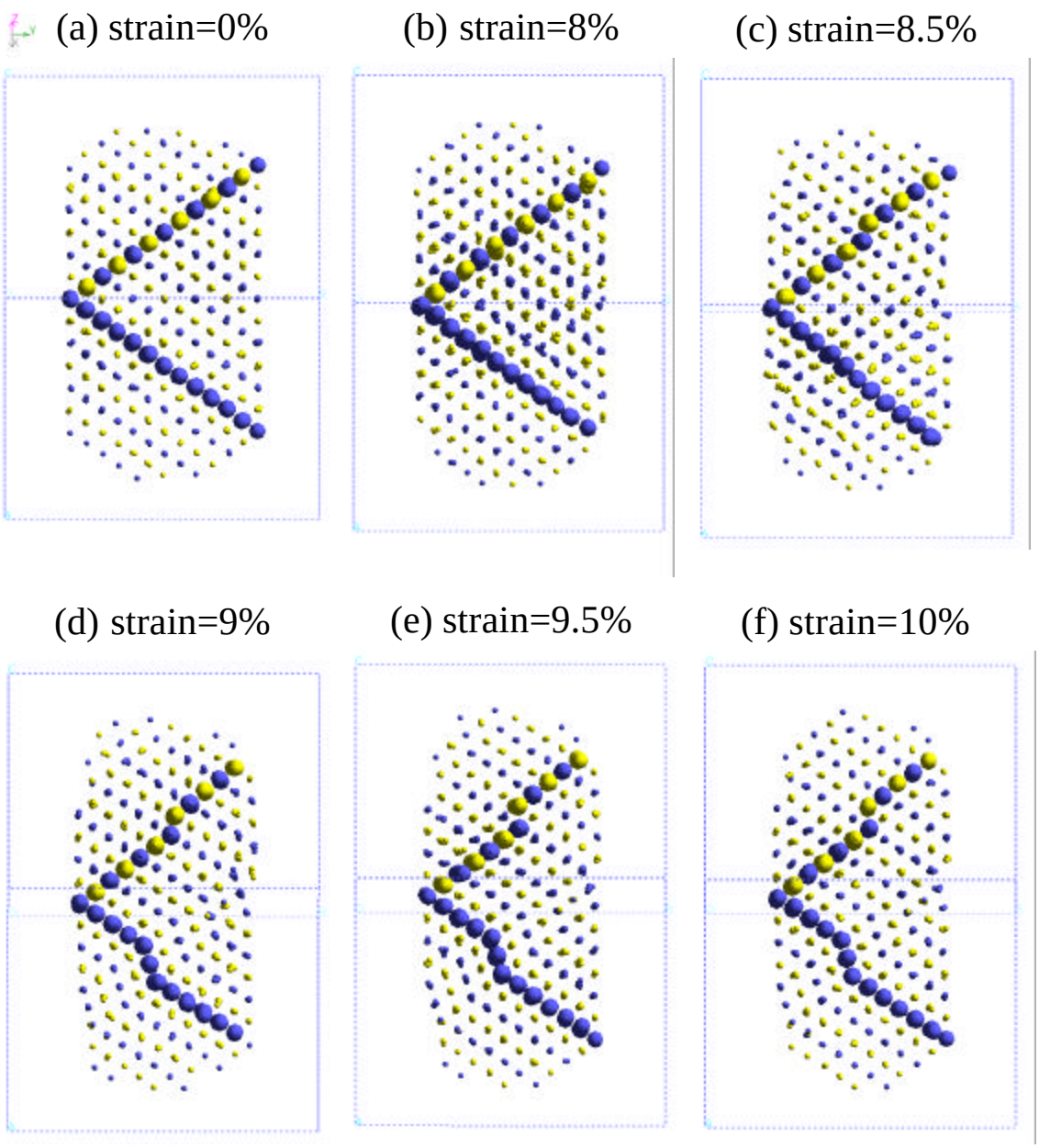

Figure 4-4. The (011) projection of the Cu single crystalline wire structure at various strain states.

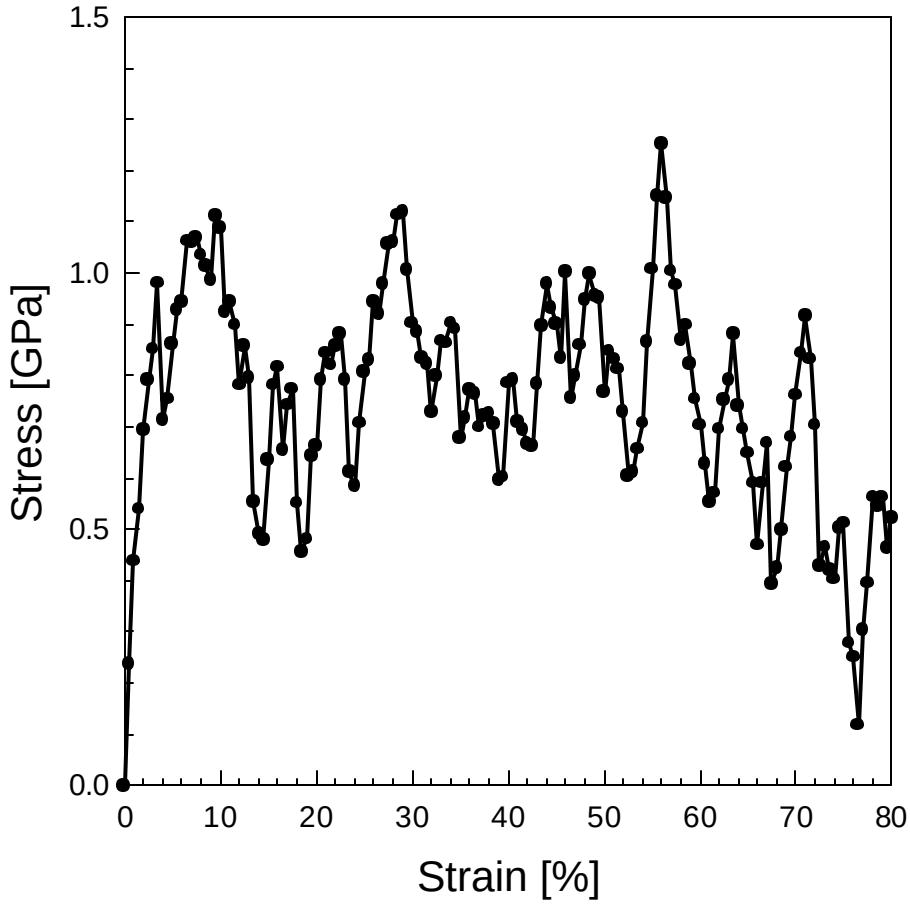

Figure 4-5. The stress-strain curve of the $Cu^{*}_{50}Cu_{50}$ amorphous nano-wire.

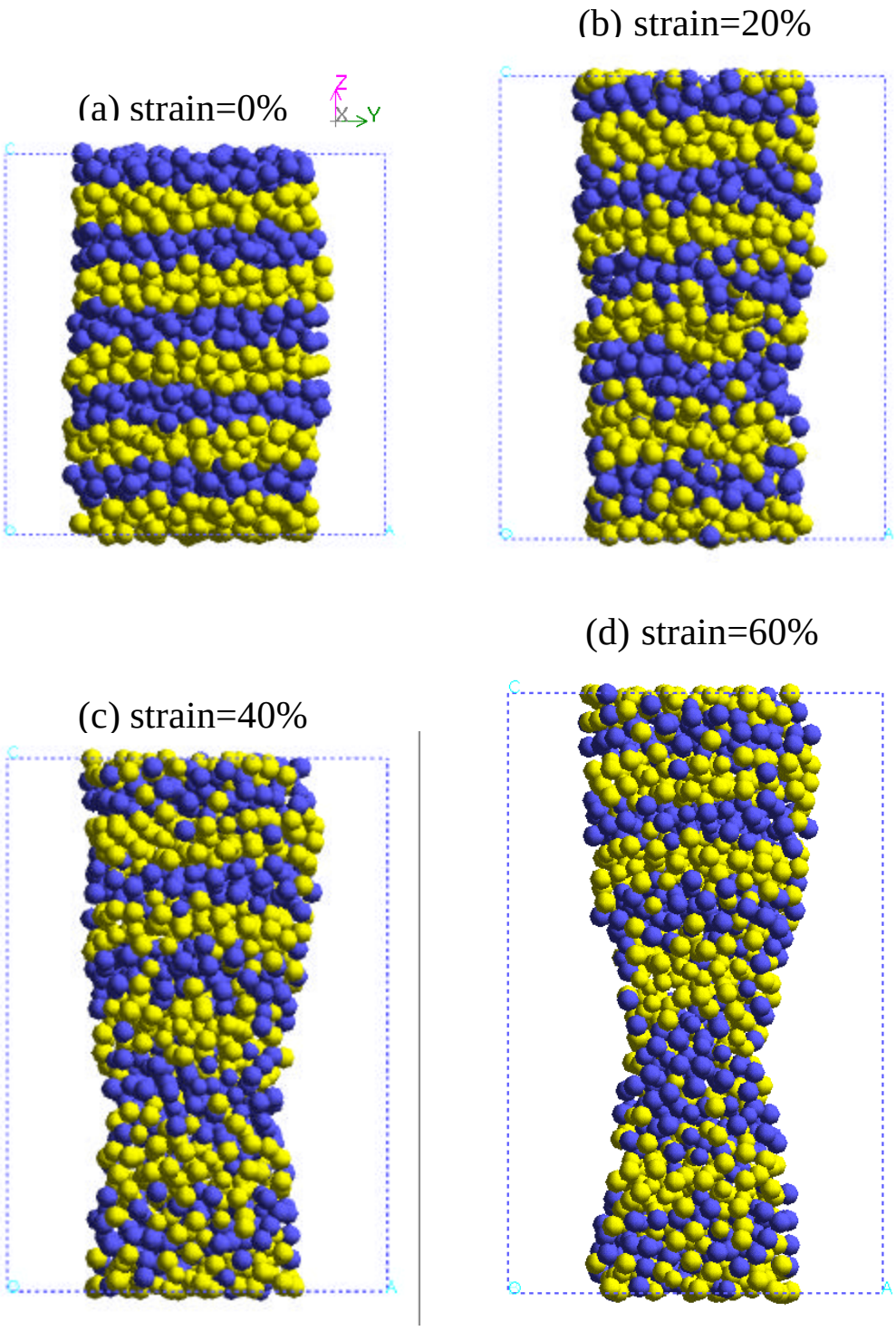

Figure 4-6. Snapshots of the $Cu^{*}_{50}Cu_{50}$ amorphous nano-wire at different strain states. Atoms are color-coded according to their z position at strain=0.0%.

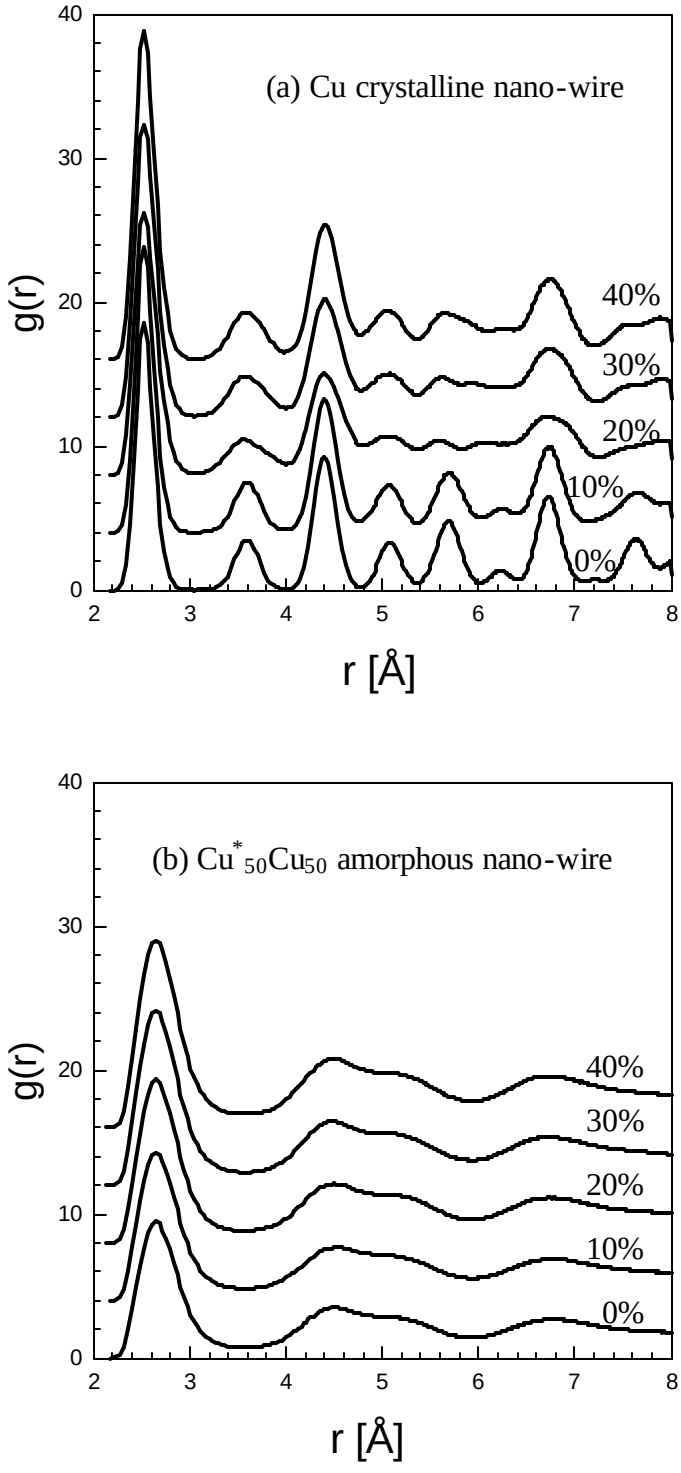

Figure 4-7. The radial distribution functions g(r) at strain=0%,10%,20%,30%, and 40%.

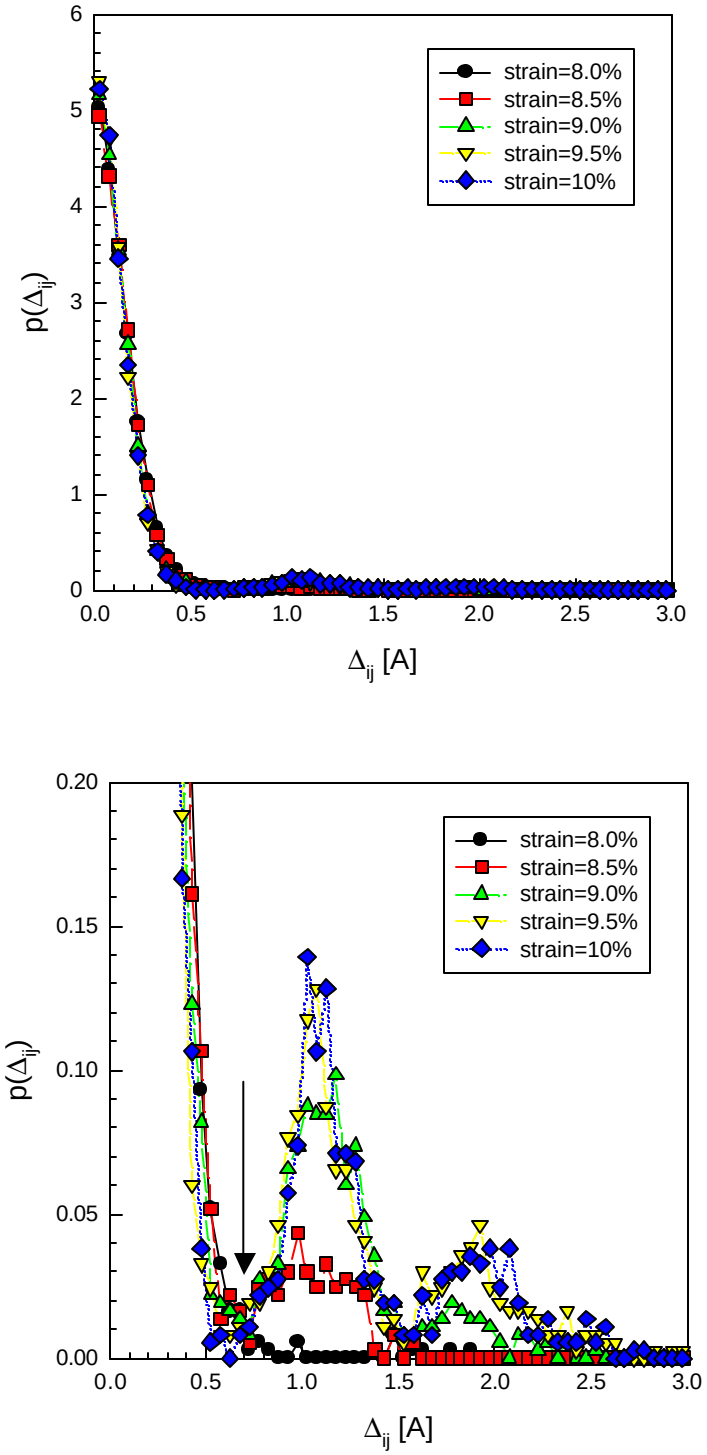

Figure 4-8. The probability distribution function of the inter-atomic distance change Δ_{ij} of the Cu crystalline nano-wire. The bottom figure is a magnification of the top figure.

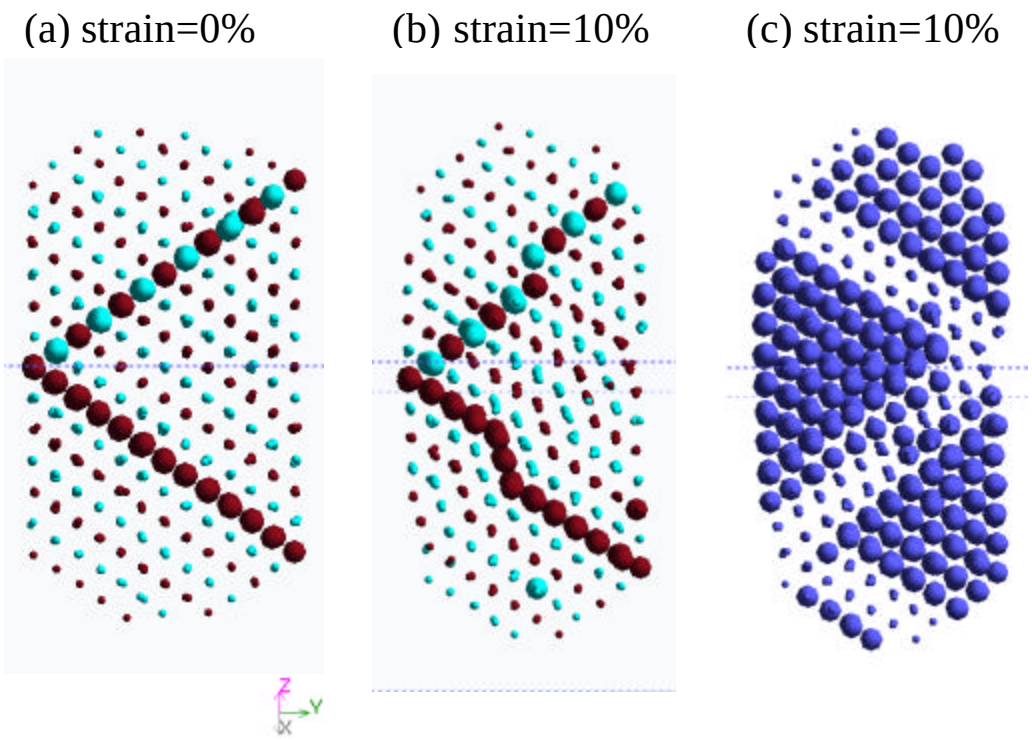

Figure 4-9. Snapshots of the Cu crystalline wire. The plastically deformed pairs are shown as small spheres and the elastically deformed pairs are shown as large spheres in (c). The plastically deformed pairs and the elastically deformed pairs are determined using Δ_{ij} parameter using a reference configuration at strain=0%.

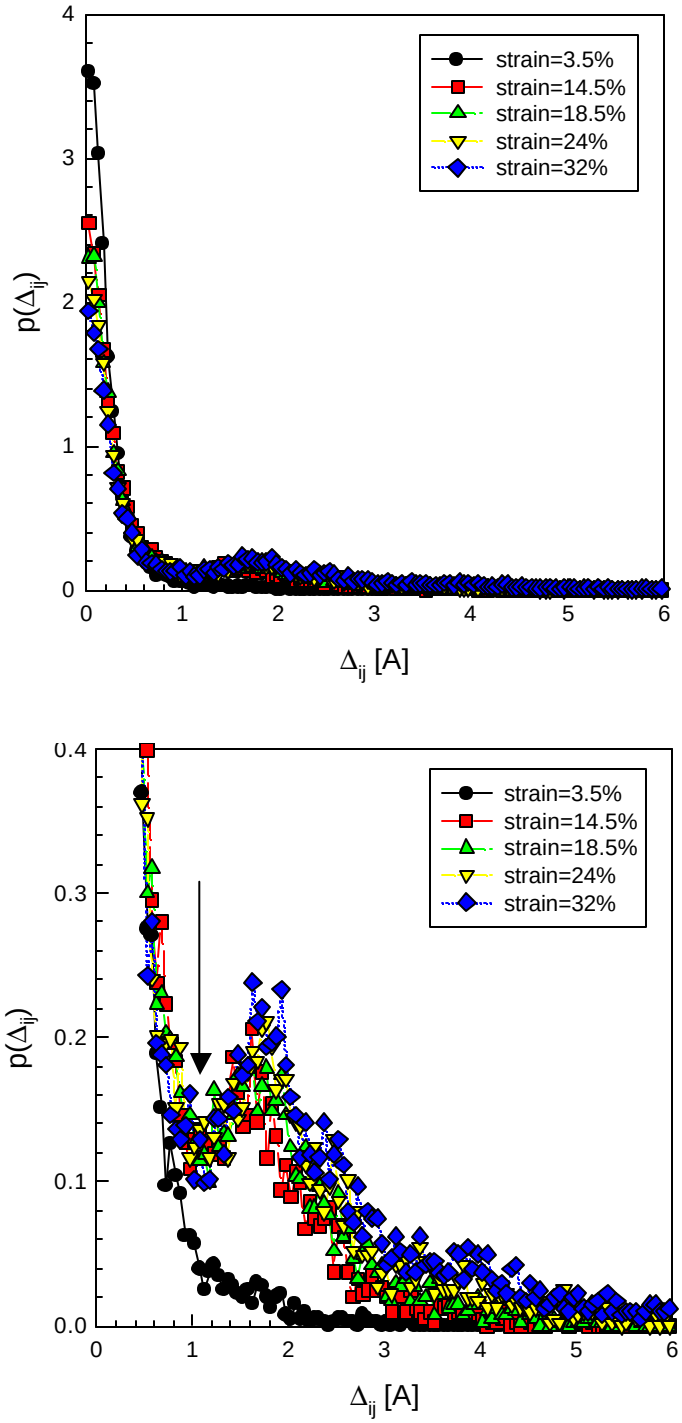

Figure 4-10. The probability distribution function of the inter-atomic distance change Δ_{ij} of the $Cu^{*}_{50}Cu_{50}$ amorphous nano-wire. The bottom figure is a magnification of the top figure.

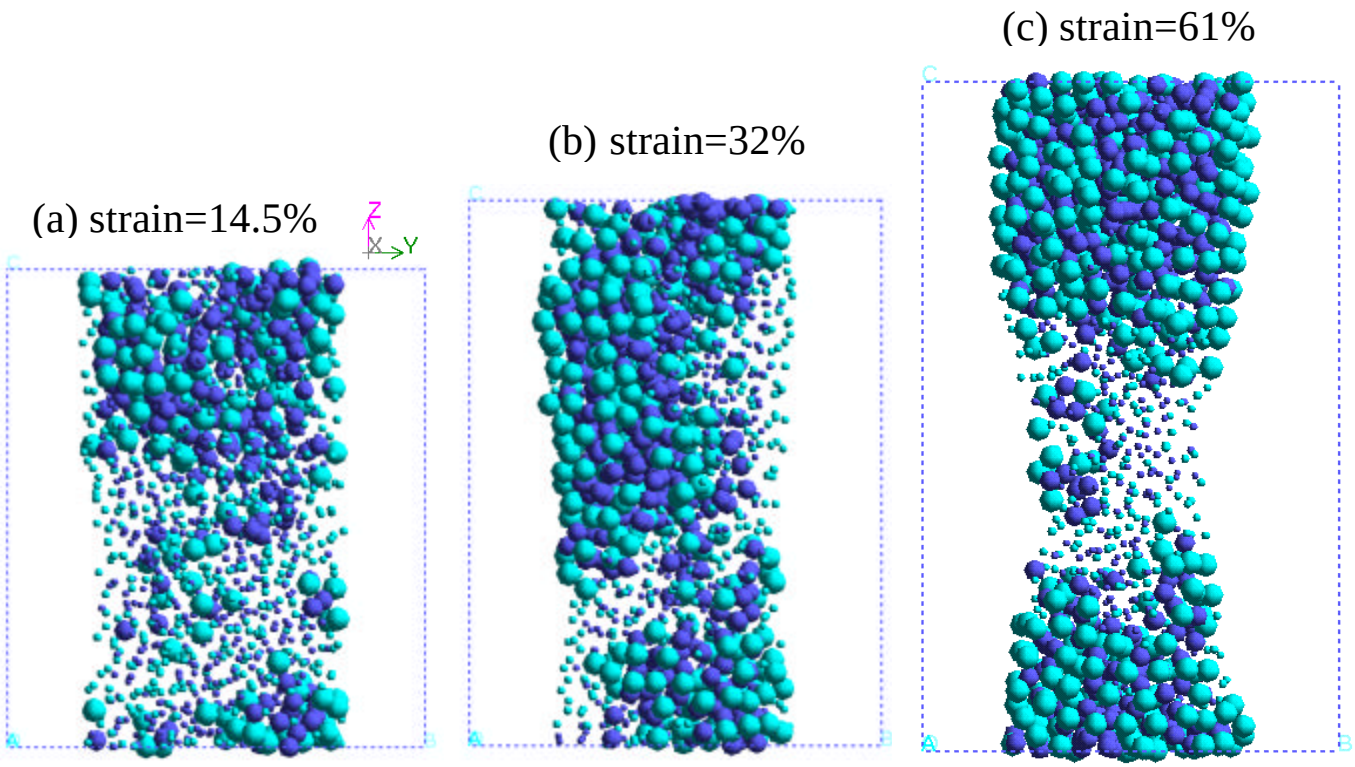

Figure 4-11. Snapshots of the $Cu^{*}_{50}Cu_{50}$ amorphous nano-wire at different strains. Different colors represent different atomic species. The plastically deformed pairs are shown as small spheres and the elastically deformed pairs are shown as large spheres. The plastically deformed pairs and the elastically deformed pairs are determined using Δ_{ij} parameter using a reference configuration. (a) 14.5% (reference configuration 0.0%). (b) 32.0% (reference configuration 24.0%). (c) 61.0% (reference configuration 52.5%).

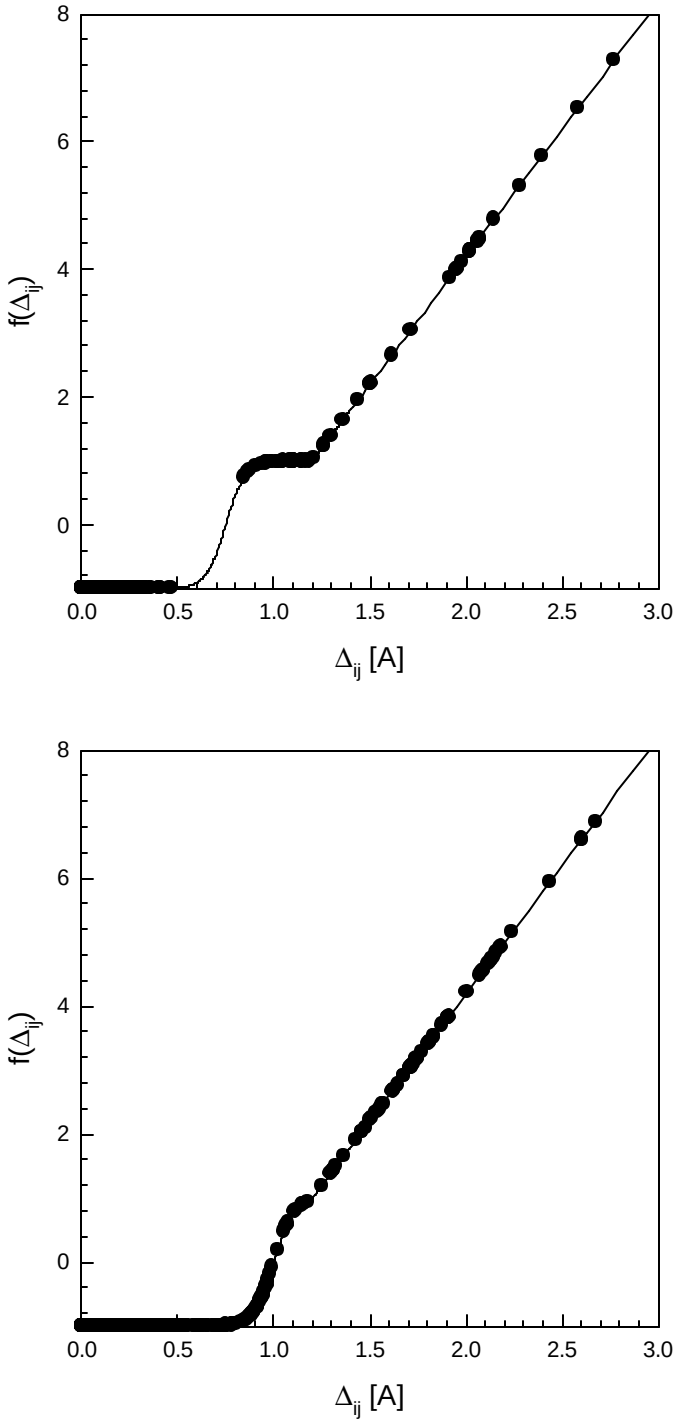

Figure 4-12. The $f(\Delta_{ij})$ used for the cluster partition processes is shown for the crystalline nano-wire (top) and the amorphous nano-wire (bottom). Each points represents a value calculated using the Δ_{ij} data points for the crystalline wire at strain=10% (top) and the amorphous wire at strain=32% (bottom).

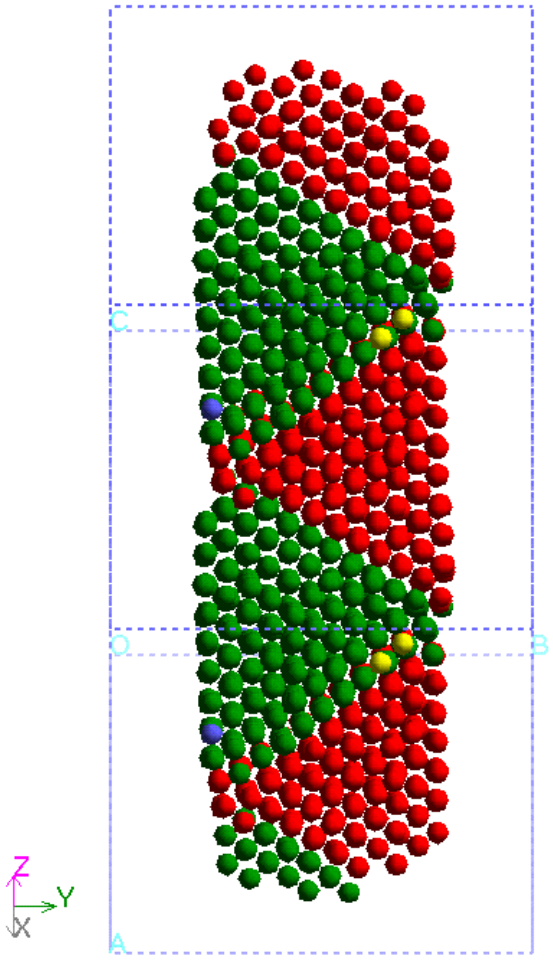

Figure 4-13. Cluster visualization of the Cu crystalline wire at strain 10.0%. The method partitions the wire into 5 clusters, with N=757, 609, 1, 2, 1 atoms, respectively. The total number of atoms in the unit cell is 1370. Two major clusters are presented here (757 and 609 atoms). The cluster with 757 atoms is shown in red and the cluster with 609 atoms is shown in green.

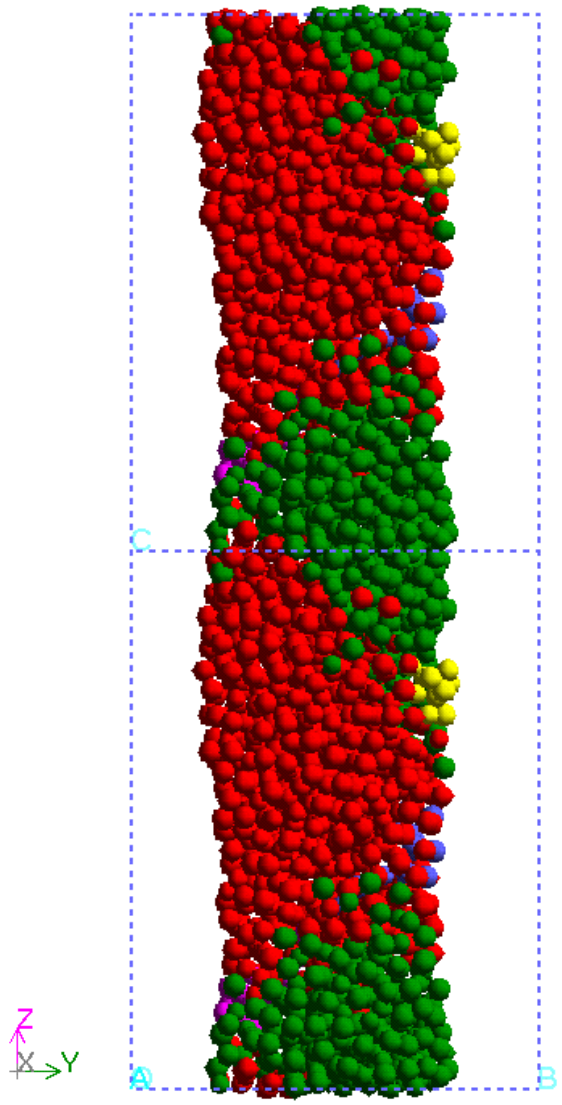

Figure 4-14. Cluster visualization of the $Cu^{*}_{50}Cu_{50}$ amorphous nano-wire at strain 32.0%. The method partitions the wire into 22 clusters, with N=839, 434, 20, 10, 18 atoms and clusters of N<10. Two major clusters are presented here (839 and 434 atoms). The cluster with 839 atoms is shown in red and the cluster with 434 atoms is shown in green.

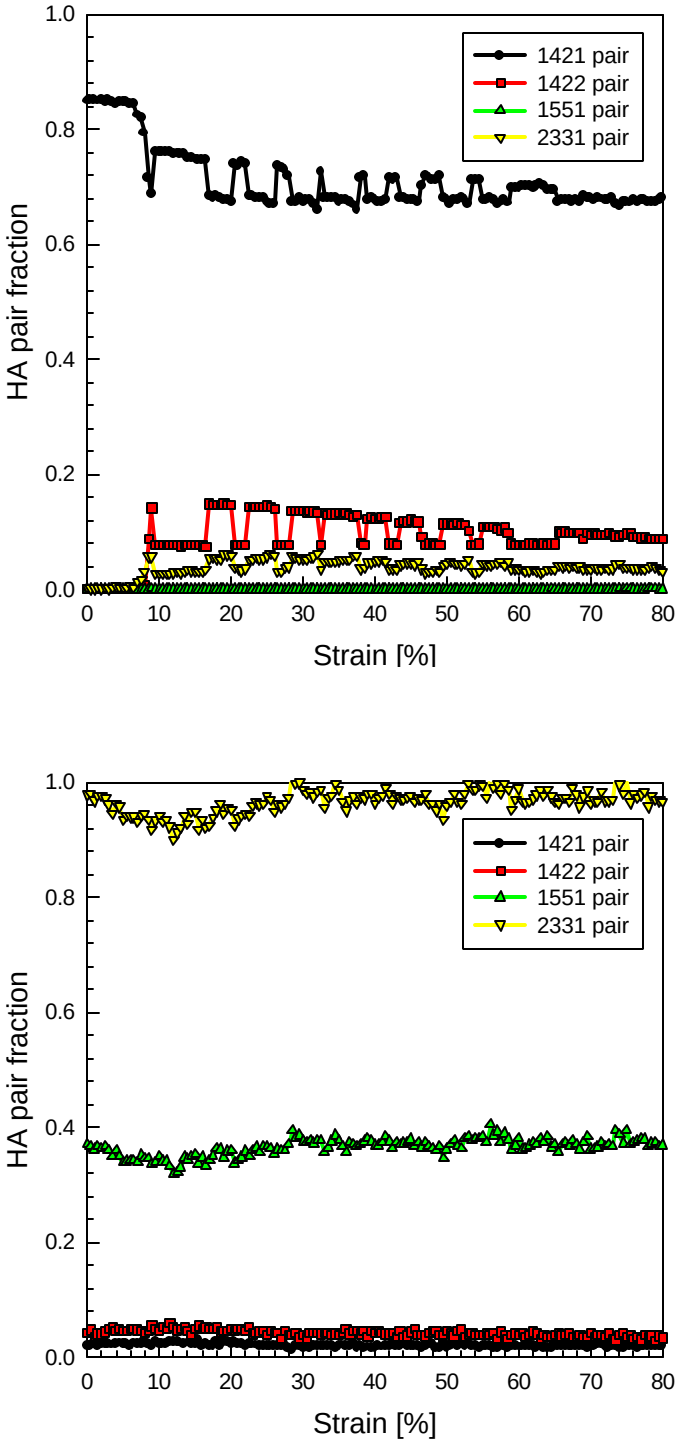

Figure 4-15. The changes of HA indexes as a function of strain for the Cu crystalline nano-wire (top) and the $Cu^{*}_{50}Cu_{50}$ amorphous nano-wire (bottom).

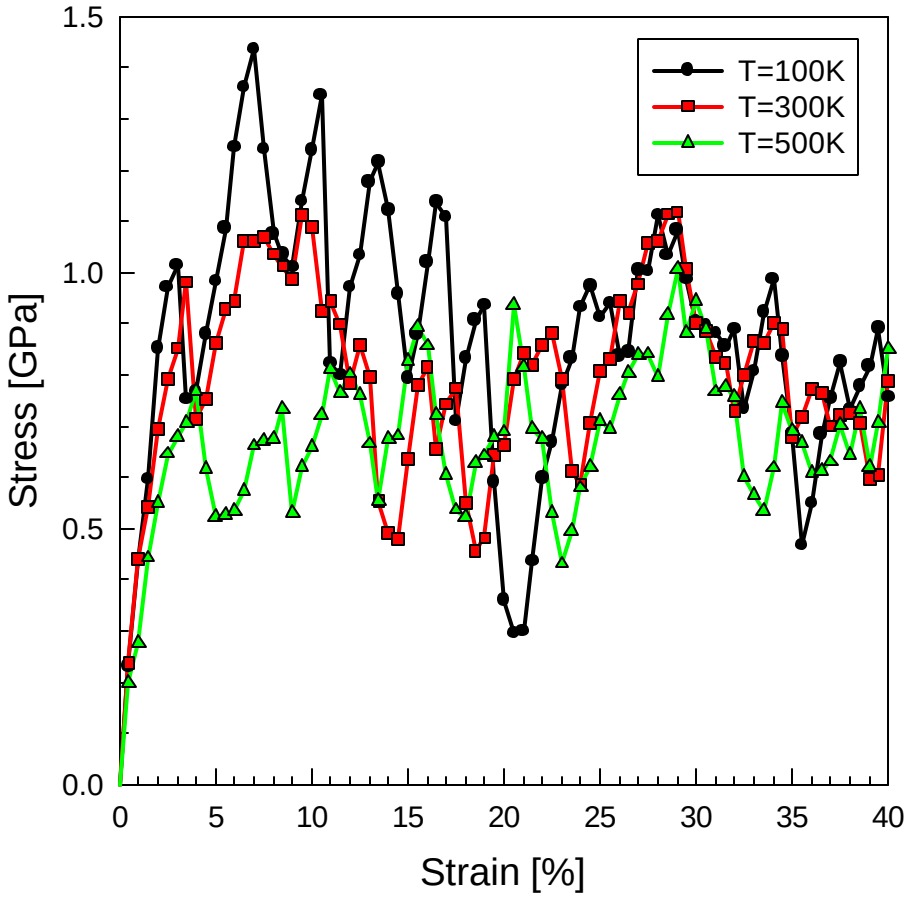

Figure 4-16. The stress-strain curve for the $Cu^{*}_{50}Cu_{50}$ amorphous nano-wire at different temperatures.

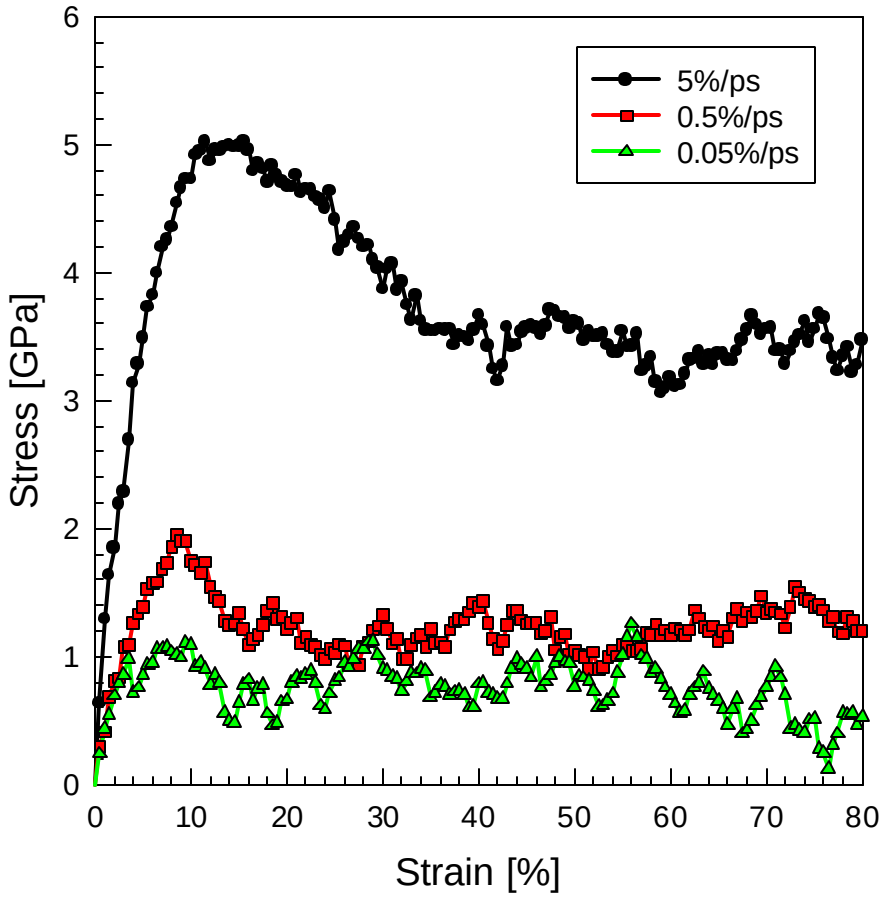

Figure 4-17. The stress-strain curves for the $Cu^{*}_{50}Cu_{50}$ amorphous nano-wire at different strain rates.

(a) notched crystalline slab

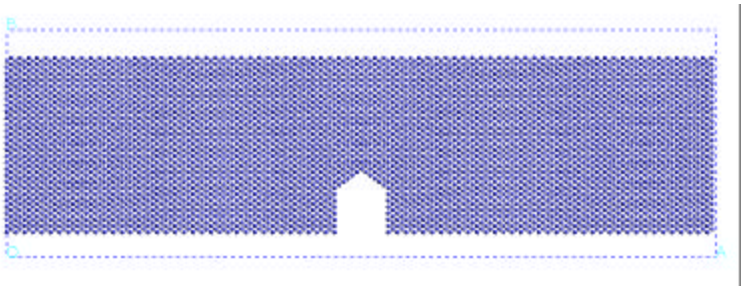

(b) after thermalization at T=300K for 5ps

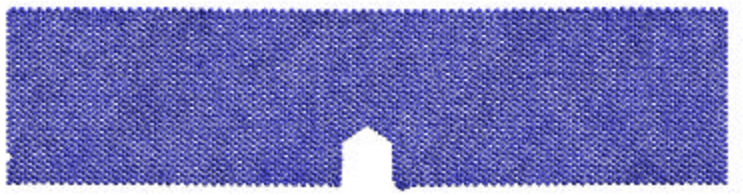

(c) notched amorphous slab

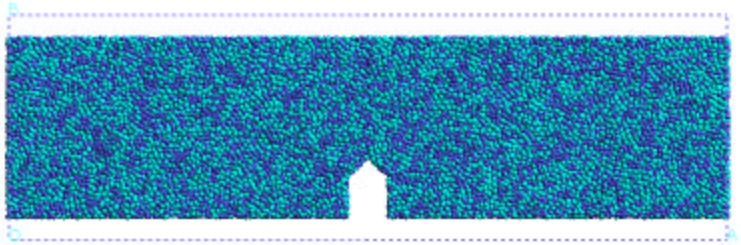

(d) after thermalization at T=300K for 5ps

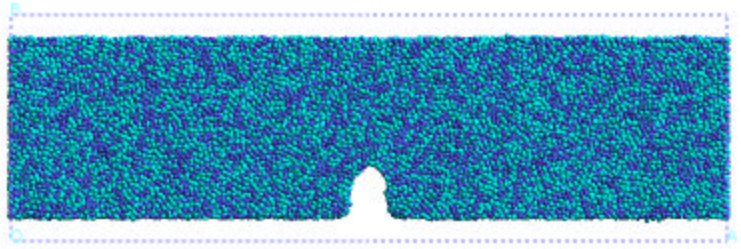

Figure 4-18 (a and b) The notched crystalline nano-slab. The cell size is 288.6Å×71.4Å×35.7Å. The crack plane is on (010) and crack front is along the [101] direction. (c and d) The notched $Cu^{*}_{50}Cu_{50}$ amorphous nano-slab. The initial cell size is 311.9Å×78.0Å×39.0Å. The crack plane is on y-z plane and crack front is along y-direction.

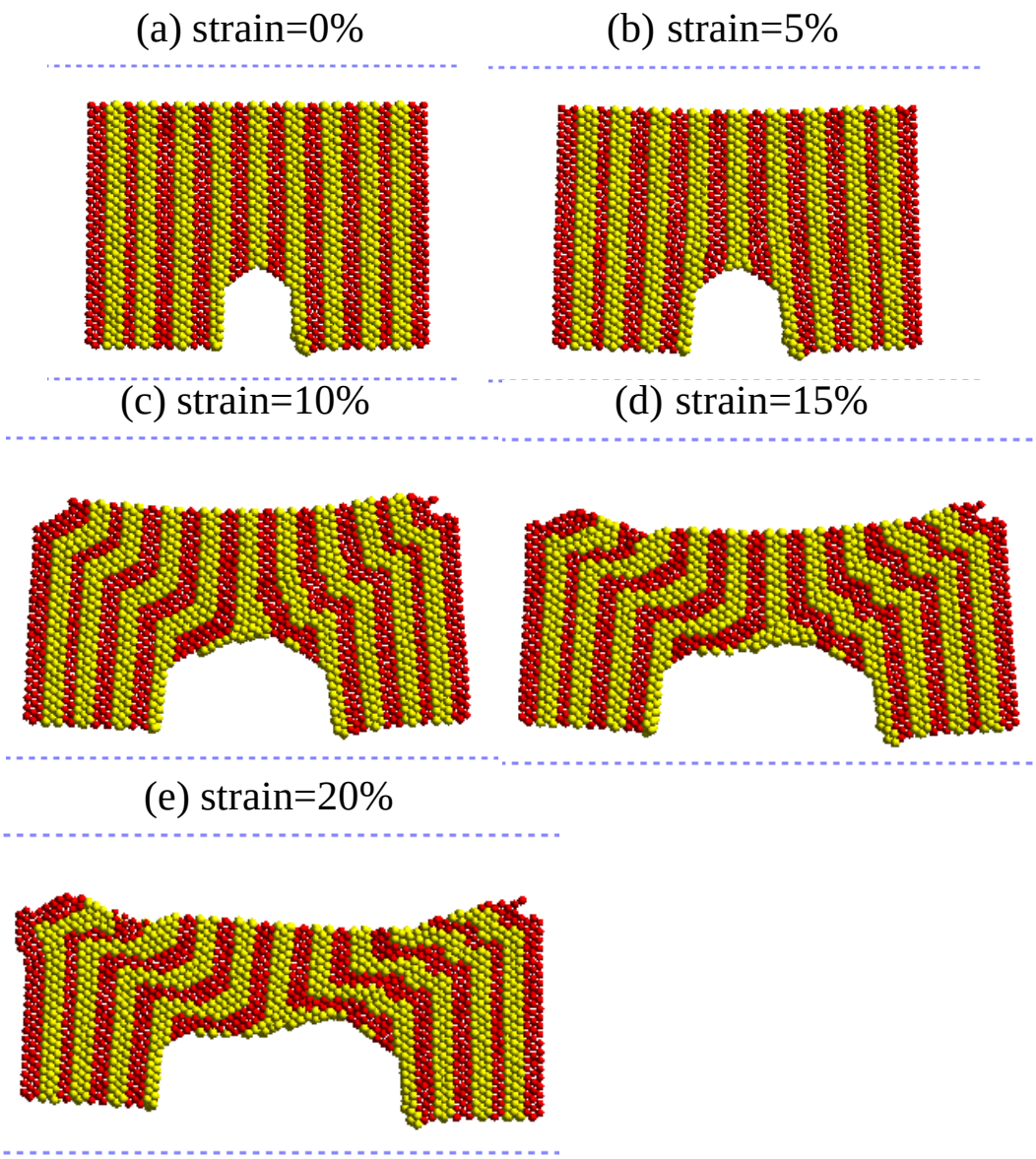

Figure 4-19. The rearrangement in atomic structure for the Cu crystalline nano-slab near the crack tip during deformation. Atoms are colored corresponding to the initial x coordinate positions. Note that the width of each colored slab does not change.

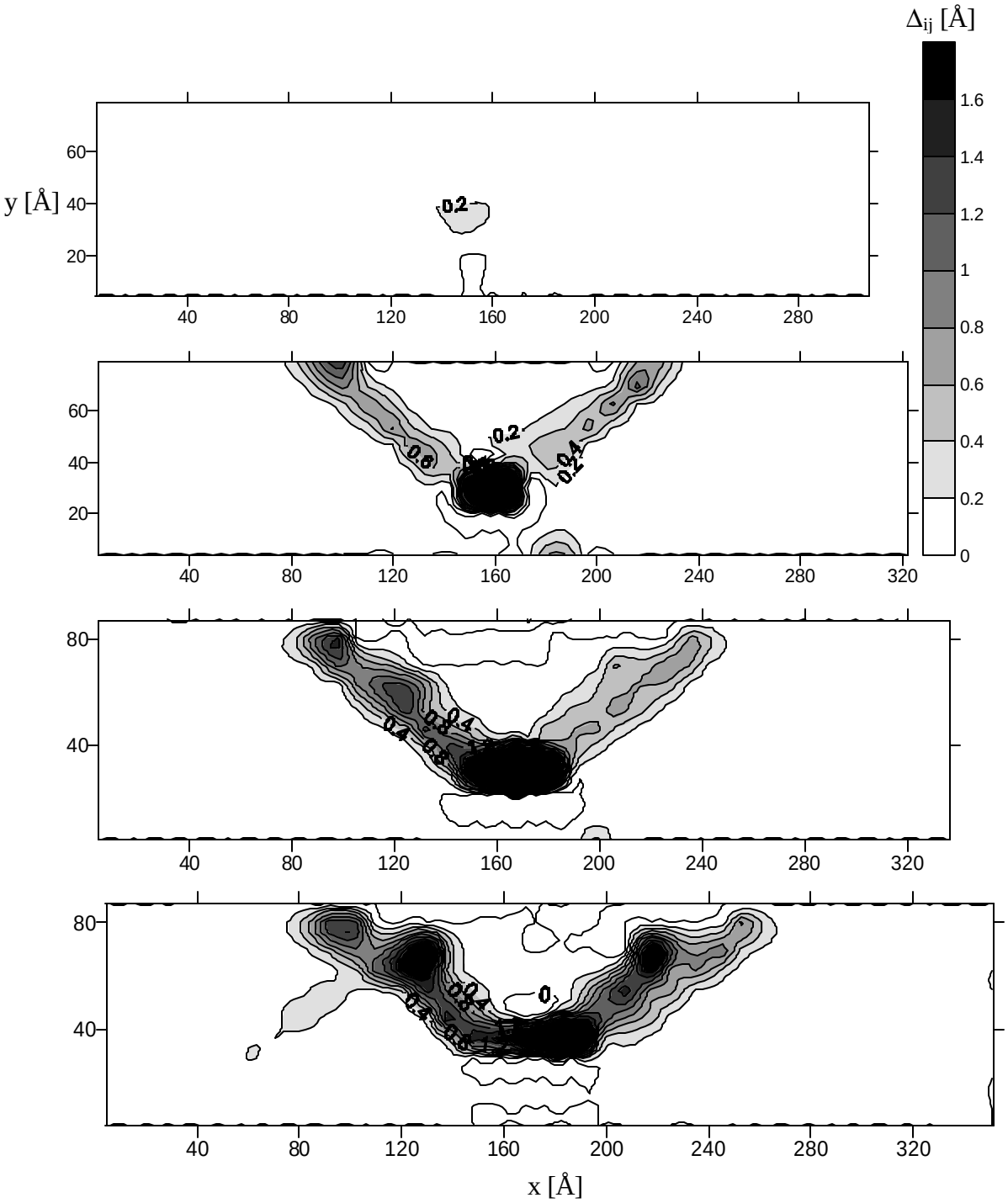

Figure 4-20. Δ_{ij} contour plots for the Cu crystalline nano-slab. From top to bottom, strain=5%, 10%, 15%, and 20%.

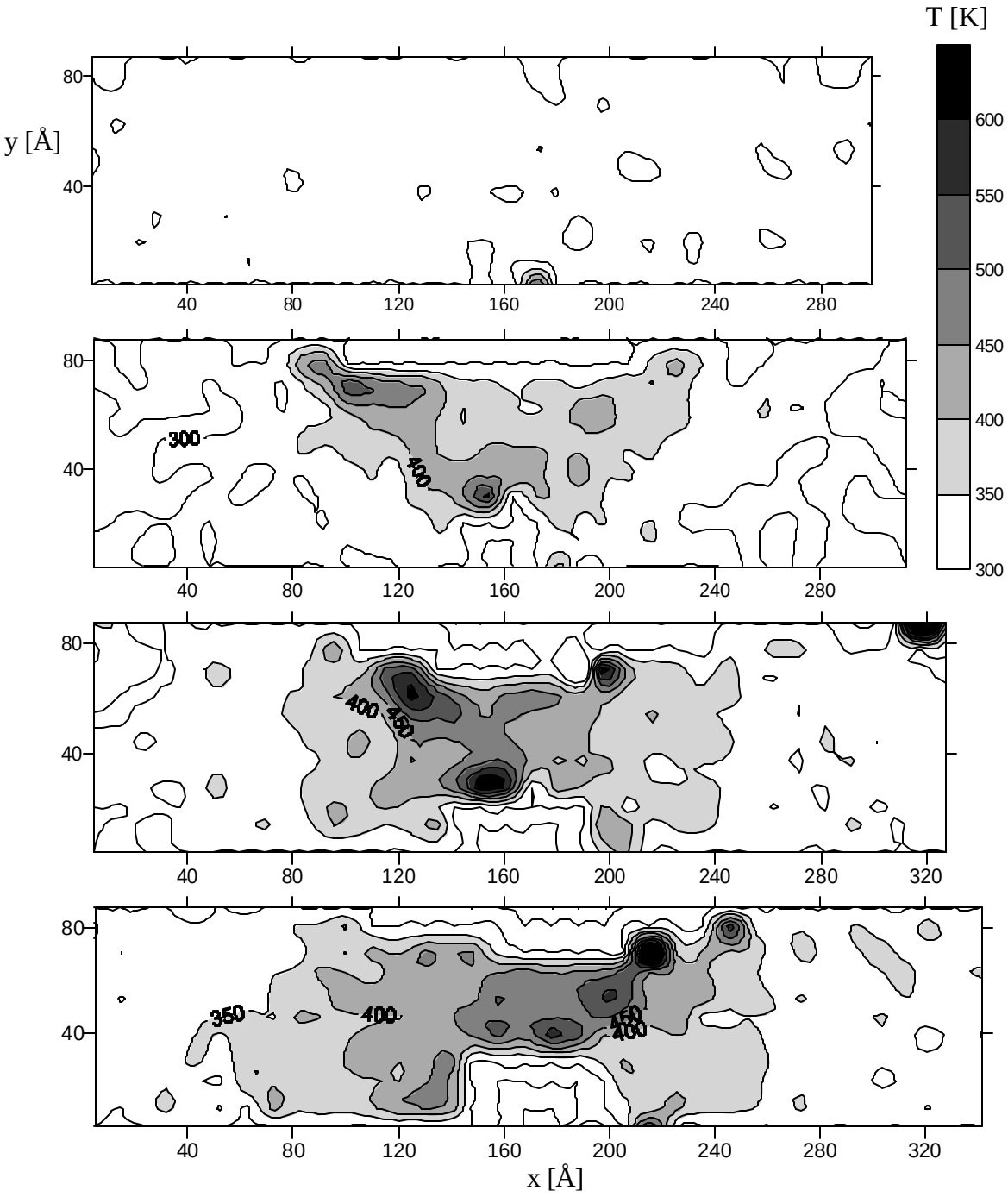

Figure 421. Local temperature plots for the Cu crystalline nano-slab. From top to bottom, strain=5%, 10%, 15%, and 20%.

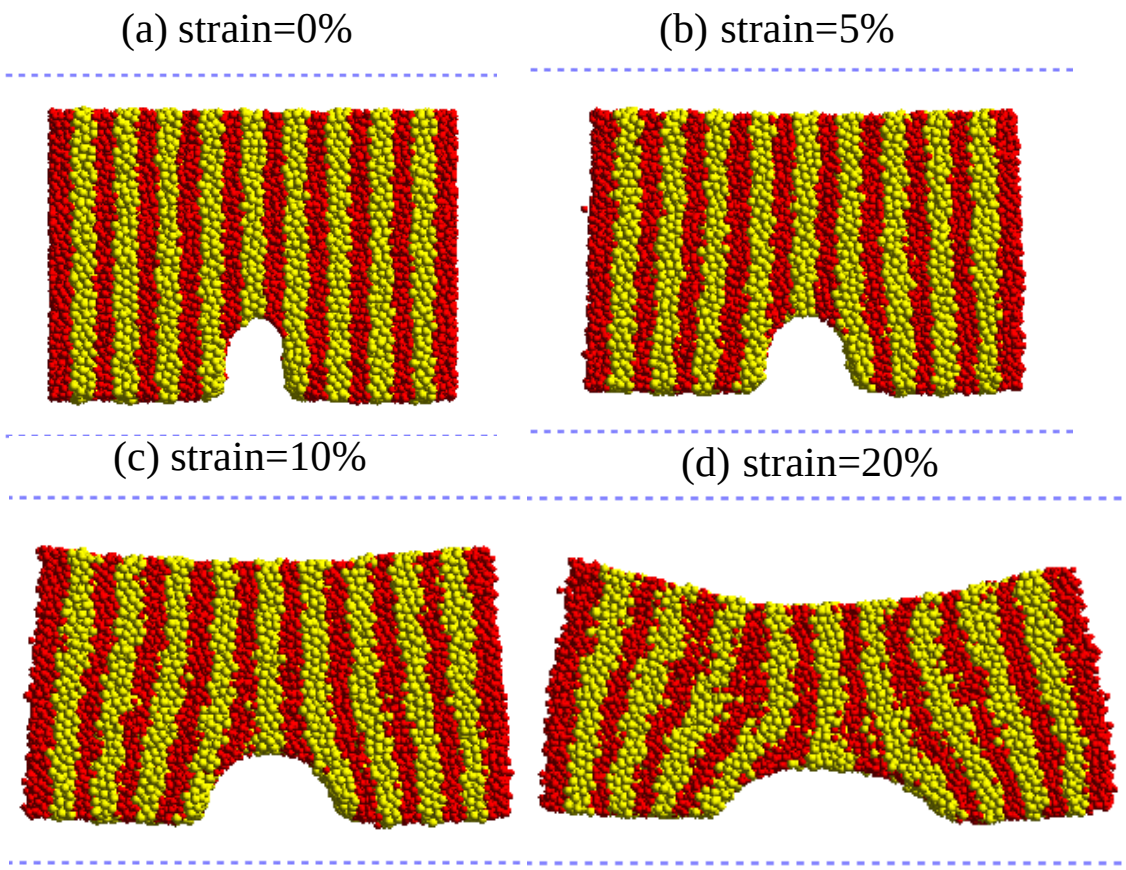

Figure 4-22. The rearrangement in atomic structure for the $Cu^{*}_{50}Cu_{50}$ glass nano-slab near the crack tip during deformation. Atoms are colored corresponding to the initial x coordinate positions. Note that the width of each colored slab increases as the strain increases, especially at the maximum stress plane (45 degrees from the crack tip).

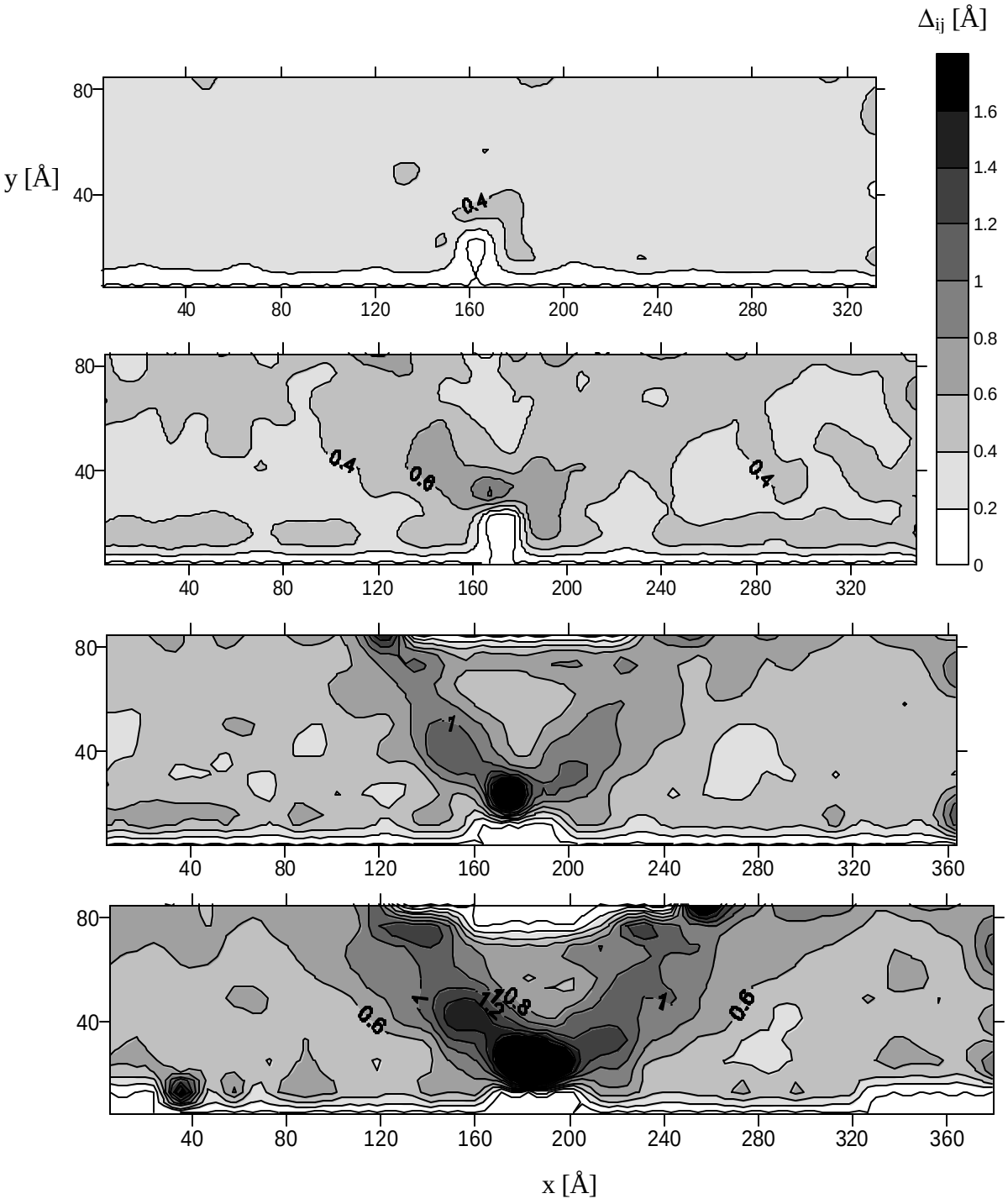

Figure 4-23. Δ_{ij} contour plots for the $Cu^{*}_{50}Cu_{50}$ amorphous nano-slab. From top to bottom, strain=5%, 10%, 15%, and 20%.

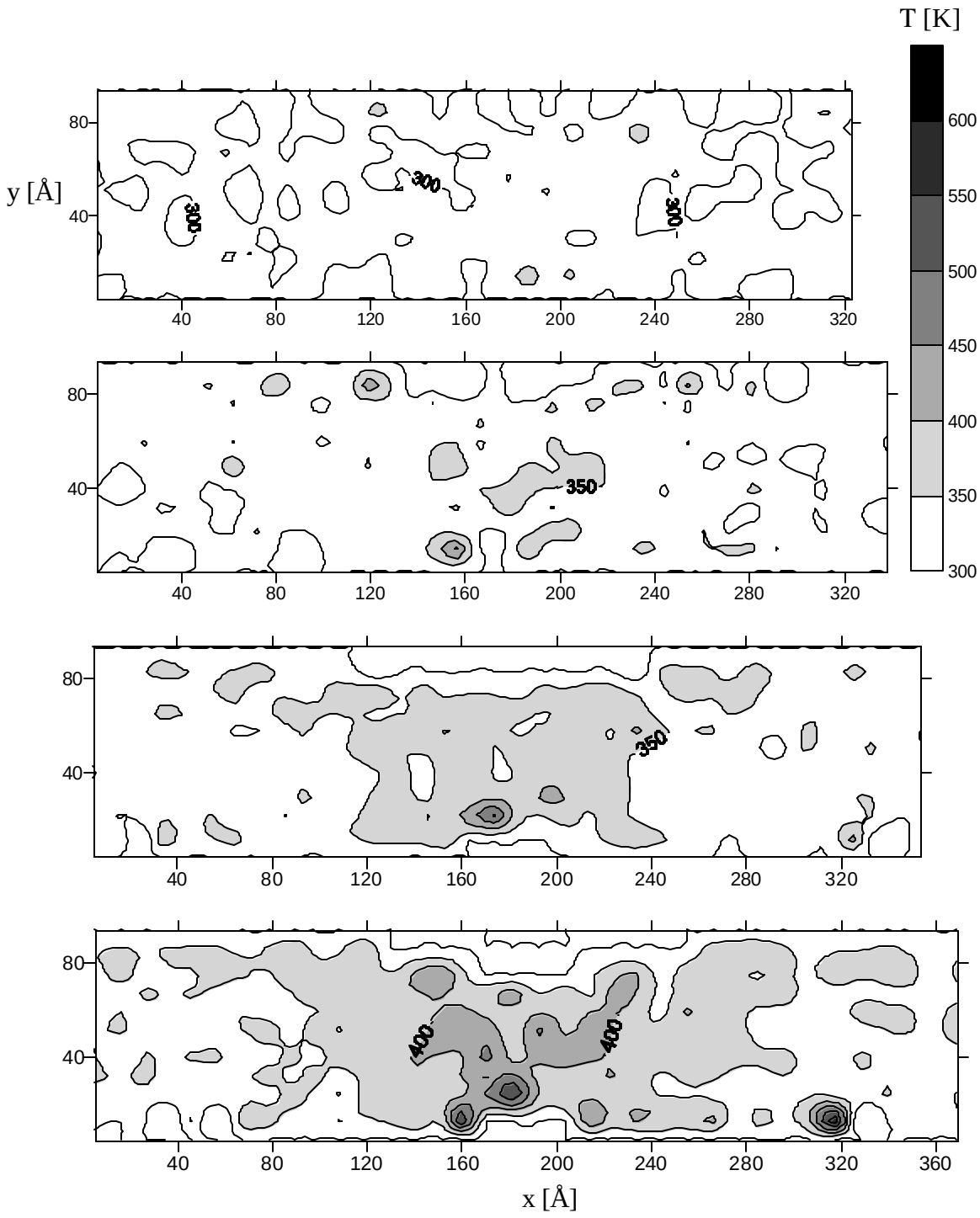

Figure 4-24. Local temperature plots for the $Cu^{*}_{50}Cu_{50}$ amorphous nano-slab. From top to bottom, strain=5%, 10%, 15%, and 20%.